Modeling for Ultrasonic Vibration-assisted Helical Grinding of SiC particle-reinforced Al-MMCs

Qilin Li[a,b]; Songmei Yuan[a,b], Bochuan Chen[a,b], Xiaoxing Gao[a,b], Zhen Li[c], Muhammad Amin[d], Andre D.L. Batako[e]

[a]School of Mechanical Engineering and Automation, Beihang University, Beijing, 100191, PR China

[b]Ningbo Institute of Technology, Beihang University, Ningbo 315832, PR China

[c]Department of Mechanics and Aerospace Engineering, Southern University of Science and Technology, Shenzhen, 518055, PR China

[d]National Centre for Physics, Islamabad, Pakistan

[e]General Engineering Research Institute, Liverpool John Moores University, Liverpool, L3 5UX, UK

Corresponding author: Songmei Yuan

Corresponding e-mail: yuansmbuaa@163.com

Corresponding tel.: +86-010-82339630

E-mail addresses of all authors:

liqilin93@buaa.edu.com;

yuansmbuaa@163.com;

brucechen@buaa.edu.cn;

gaoxiaoxing83@buaa.edu.cn;

liz33@sustech.edu.cn;

aminbuaa@yahoo.com;

a.d.batako@ljmu.ac.uk;

Abstract： Silicon carbide (SiC) particle-reinforced aluminum matrix (SiC_p/Al) composites have continuously increased applications in abundant industries due to their superior mechanical properties. However, such composites have issues achieving desired machinability and quality standard due to the presence of SiC particles which is the main hindrance to their applications. In this paper, the methodology of ultrasonic vibration-assisted helical grinding (UVHG) of SiC_p/Al composites has been applied to achieve to desired quality and efficiency for such composites. Then a mechanical cutting force model was developed to predict grinding forces. The grinding force was separated into friction force, plastic deformation force, and fracture force on account of the material removal mechanism. The undeformed chip thickness and cross-sectional area were calculated for the grinding force of a single diamond abrasive grit and then extended to the whole tool. By considering the acoustic softening effect of reduction of deformation stress caused by ultrasonic vibration, the acoustic softening coefficient was first proposed in the model to correct the impact of the ultrasonic vibration for properties of SiC_p/Al composites. The experimental machining (UVHG) was carried out considering the different groups of experiments. The experimental results found agreed with the predicted values of cutting forces. The prediction deviation of the model was 5.07%, which could provide further guidance for the grinding process optimization of SiC_p/Al composites. The novel cutting force predicted model and proposed machining methodology could be applied to machining SiC_p/Al composites at the industry level and further research work.

Keywords: SiC_p/Al composites; Ultrasonic vibration-assisted helical grinding; Undeformed chip thickness; Undeformed chip cross-sectional area; Force model; Acoustic softening.

Nomenclature	
UVHG	ultrasonic vibration-assisted helical grinding
l	bottom surface diagonal length of diamond grit on the tool (μm)
l'	distance between every diamond grit on the tool (μm)
δ	exposed height of the diamond grit (μm)
α	apex angle of the diamond grit (rad)

l_{SiC}	standoff distance of SiC particles (μm)
d_{SiC}	diameter of SiC particles (μm)
f	frequency of ultrasonic vibration (Hz)
A	maximum amplitude (μm)
Δh	instantaneous ultrasonic vibration displacement (μm)
r	radius of the diamond abrasive tool (mm)
R	radius of the machined hole (mm)
C	concentration of diamond grits (mm^{-2})
n_s	spindle speed (rpm)
f_r	feed rate of tool ($mm \cdot min^{-1}$)
$\boldsymbol{v_s}$	linear velocity of tool ($m \cdot min^{-1}$)
$\boldsymbol{v_r}$	axial feed speed/feed movement in the z-direction ($m \cdot min^{-1}$)
$\boldsymbol{v_t}$	radial feed speed/feed movement on the xy-plane ($m \cdot min^{-1}$)
η_n	center angle of every two side diamond grit (rad)
θ_t	center angle of every two bottom diamond grit (rad)
m	number of active side diamond girts on the tool side face involved in grinding
n	number of active bottom diamond girts on the tool side face involved in grinding
A_c	end face area of the tool involved in grinding (mm^{-2})
h_s	undeformed chip thickness of side grinding (μm)
h_t	undeformed chip thickness of end grinding (μm)
a_s	cutting depth of side grit (μm)
a_e	cutting depth of bottom grit (μm)
a_p	axial feed depth per helical revolution (μm)
S_l	undeformed chip cross-sectional area of side grit (mm^{-2})
S_e	undeformed chip cross-sectional area of bottom grit (mm^{-2})
$\boldsymbol{F}$	total grinding force (N)
$\boldsymbol{F}_{SG}$	side grinding force (N)
$\boldsymbol{F}_{EG}$	end grinding force (N)
$\boldsymbol{f}_{SGP}$	plastic deformation force of aluminum alloy matrix (N)
$\boldsymbol{f}_{SGF}$	fracture force of SiC particles (N)
$\boldsymbol{f}_{EGf}$	friction force (N)
σ_m	contact stress (MPa)
σ_s	yield limit of the composites (MPa)
σ_p	fracture stress of SiC particle (MPa)
E	elastic modulus of SiC (MPa)
μ_s	friction coefficient of side grit
μ_e	friction coefficient of bottom grit
k_1	coefficient to correct the number of active side diamond girts involved in grinding
k_2	coefficient to correct the number of active end diamond girts involved in grinding
v	Poisson's ratio of SiC
h_{tool}	active diamond abrasive grits length of the tool (mm)
ψ	softening coefficient caused by ultrasonic vibration
K_{IC}	fracture toughness of the SiC ($MPa \cdot m^{0.5}$)
H_V	Vickers hardness of SiC

1. Introduction

SiC particle-reinforced metal matrix composites (PRMMCs) have got paramount importance and widely increased applications in aerospace, semiconductor packaging, and other industrial fields [1,2] because of their excellent properties [3]. However, the machinability and quality of machining for such materials were found to be lower for such composite materials, especially materials having high volume fraction (≥45%) silicon carbide particle reinforced aluminum matrix composites (SiC_p/Al). Due to the addition of SiC hard particles in SiC_p/Al composites, excessive cutting forces, high cutting temperature, and severe tool wear were found [4]. These composites contain a high-volume fraction of SiC particles with high hardness and wear resistance. In addition, due to the plasticity of the aluminum alloy matrix, SiC_p/Al often adheres to the tool surface during machining and deteriorates the cutting environment [5]. Therefore, SiC_p/Al composites are recognized in the industry as typically difficult-to-machining hard and brittle composite materials. As an effective

approach to processing hard and brittle materials, ultrasonic vibration-assisted machining (UVAM) can reduce the cutting force in the machining process and improve the machining quality and tool life by applying high-frequency vibration to the tool in the machining process [6]. During the machining process, the cutting force has a direct impact on the material removal process [7,8], tool life [9,10], and surface integrity [11,12]. By predicting and adjusting the cutting force in the processing, machining efficiency and quality can be improved by optimizing related parameters.

Due to severe and rapid tool wear in the machining of SiC_p/Al composites, cemented carbide tools and even diamond-coated tools commonly used in industry are challenging to complete the machining process [13]. Cubic boron nitride (CBN), polycrystalline diamond (PCD), and single crystal diamond (SCD) cutting tools show the advantages of processing high volume fraction SiC_p/Al composites [14,15,16,17]. But their high cost has become another major obstacle to the popularization and application of the composites. To seek efficient and low-cost solutions, some scholars cast their attention on some non-traditional machining technology [18], such as electrical discharge machining (EDM) [19,20], laser beam machining (LBM) [21,22,23], abrasive water jet machining (AWJM) [24] and so on. However, these non-traditional technologies have inevitably shown some defects and relatively low efficiency.

In ultrasonic vibration-assisted machining, ultrasonic vibrations are introduced in the machining process, and the advantages of low cutting force, low heat, less tool wear, and better geometrical accuracy can be achieved. Kadivar et al. [25] investigated that the cutting force was significantly reduced under ultrasonic vibration-assisted drilling. Zhou and Lu et al. [26,27] revealed that the tool wear markedly reduced during the ultrasonic vibration-assisted turning of SiC_p/Al. Kang et al. [28] found that the grinding force of ultrasonic vibration-assisted grinding of 55vol.% SiC_p/Al is 35–50% lower than that of conventional grinding. The current research on ultrasonic vibration-assisted machining of SiC_p/Al composites mainly focuses on material removal mechanisms [29,30] and subsurface damage (SSD) [31]. However, the research on the machining process of UVHG of SiC_p/Al composites has not been reported yet. By applying ultrasonic vibration to the relatively low-cost diamond abrasive tools and feeding the tools in a way similar to helical milling [32], UVHG can achieve high-quality, high-efficiency, and low-cost machining SiC_p/Al composites.

The study of cutting forces can help us to optimize the input parameters of ultrasonic vibration machining. Pei et al. [33] proposed a mechanistic cutting force model for rotary ultrasonic machining (RUM) by considering brittle fracture as the primary mode for material removal. Feng et al. [34,35] also established a cutting force model for K9 glass and C/SiC composites based on brittle fracture theory. Zheng et al. [36] proposed an ultrasonic vibration-assisted side grinding of ceramics considering both ductile and brittle fracture removal mechanisms. Cong et al. [37,38] presented a force model of RUM for carbon fiber reinforced plastics (CFRP) composites for both brittle fracture and ductile-brittle transition. The grinding force model of SiC_p/Al composites, considering the plastic deformation, brittle fracture, and debonding, was first proposed by Bao et al. [39]. Zhou et al. [40] divided the grinding force into side grinding force and end grinding force for grinding SiC_p/Al composites. However, these force models ignore the influence of ultrasonic vibration on the properties of materials.

The study and literature review found that previous research focused on stress superposition or dislocation diffusion caused by ultrasonic vibration can lead to acoustic softening [41,42,43,44] and skin effect [45,46] on materials. Pandey et al. [47] developed a physics-based force model for ultrasonic-assisted milling of Al6063 alloy by applying acoustic softening. Zhao et al. [48] established a model for ultrasonic-assisted drilling of titanium alloy, and the acoustic softening effect was presented. However, the research on force prediction of UVHG for high-volume fraction SiC_p/Al

composites is still blank. Also, the developed cutting force models usually do not consider the influence of ultrasonic vibration on material deformation and material properties for other composites.

In this research work, a mechanistic-based grinding force prediction model is developed for ultrasonic vibration-assisted helical grinding of SiC_p/Al composites. The undeformed chip thickness (UCT) and undeformed cross-sectional area (UCA) are calculated. The grinding force model of a single diamond abrasive grit is built by considering the plastic deformation force, brittle fracture force, and friction force generated by grinding high-volume fraction SiC_p/Al composites. An ultrasonic vibration compression test corrects the influence of acoustic softening induced by ultrasonic vibration on material properties. And the sum of the grinding force of active grits on diamond abrasive tools is taken as the grinding force during UVHG of SiC_p/Al composites. Then the measured grinding force values obtained from the experiment are compared with predicted grinding force values to validate the developed model.

This paper is organized into five sections. After this introduction section, the grinding force prediction model is developed in section 2. In section 3, the experimental UVHG is carried out for SiC_p/Al composites, and the data acquired is reported. The results and discussion are mentioned in section 4. Finally, the conclusions have presented in section 5.

2. Development of force model

The UVHG process of SiC_p/Al composites is shown in **Fig.1**. The ultrasonic vibration is up and down along the axial direction of the tool. During ultrasonic machining, the material removal contains two processes: grinding of the side grit (side grinding) and grinding of the bottom grit (end grinding). Thus, the cutting force of the helical grinding process can be separated into side grinding force $\boldsymbol{F}_{SG}$ and end grinding force $\boldsymbol{F}_{EG}$. To calculate as close to the machining process as possible, the model needs to introduce several assumptions and simplifications：

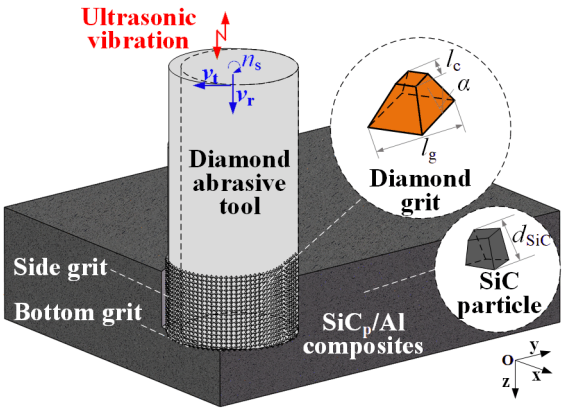

Fig.1. UVHG process of SiC_p/Al composites

(1) The diamond abrasive grits are considered rigid bodies distributed evenly on the tool with uniform size. Each abrasive grit is considered to be approximately a regular tetrahedron shape, with a base width of l_g and a top width of l_c. The angle complementary to the angle between the side and base (the rake angle) is α.

(2) The SiC particles are distributed evenly with standoff distance l_{SiC} in the material with a similar shape, and the diameter is d_{SiC}.

(3) The friction between the diamond grits and materials appears as sliding friction. The influence of temperature changes is ignored.

(4) Only the stable machining process is considered. The model does not take into account the hole-in and hole-out stages. Also, the ultrasonic vibration maintains a constant frequency f and amplitude

A. The bouncing of abrasive grits is not taken into consideration.
(5) The debonding of SiC particles is ignored, considering the size ratio of diamond grits to SiC particles, which means the particle fracture is the main form of particle damage.
(6) Taking into account the small abrasive grit edge radius, the ploughing force is not considered in this model.

2.1 Active diamond abrasive grits on cutting tools

The diamond abrasive tool discussed in this research is a cylindrical electroplated diamond grinding rod (**Fig.2a**). As shown in **Fig.2b**, the diamond abrasive grits are distributed on the tool's side face and bottom face. The Cartesian coordinate O-xy is set up at the center of the side and bottom surface to locate the diamond abrasive grits' position. The radius of the tool is r. The eccentric radius of the tool during helical grinding is r'. Divide the tool's bottom surface into j regions according to different positions from the center axis of the tool. Assign sequential numbers 1, 2, ..., i to the abrasive gritss within each region, where i and j is the natural numbers. Thus, P_{ij} represents the i^{th} side abrasive grit in j^{th} element, which j=k（j_{max}） for the side abrasive grit. Q_{ij} represents the i^{th} bottom abrasive grit in j^{th} element. $r_{i,j}$ is the distance the grit to the center of the tool. $H_{i,j}$ is the exposed height of the diamond abrasive grit of the i^{th} grit in j^{th} element For each diamond abrasive tool, the exposed height $H_{i,j}$, the average spacing between every abrasive grits L_s, the base width of diamond grit l_g, and the top width (equals to the width of the cutting edge) of l_c need to be obtained through measurement.

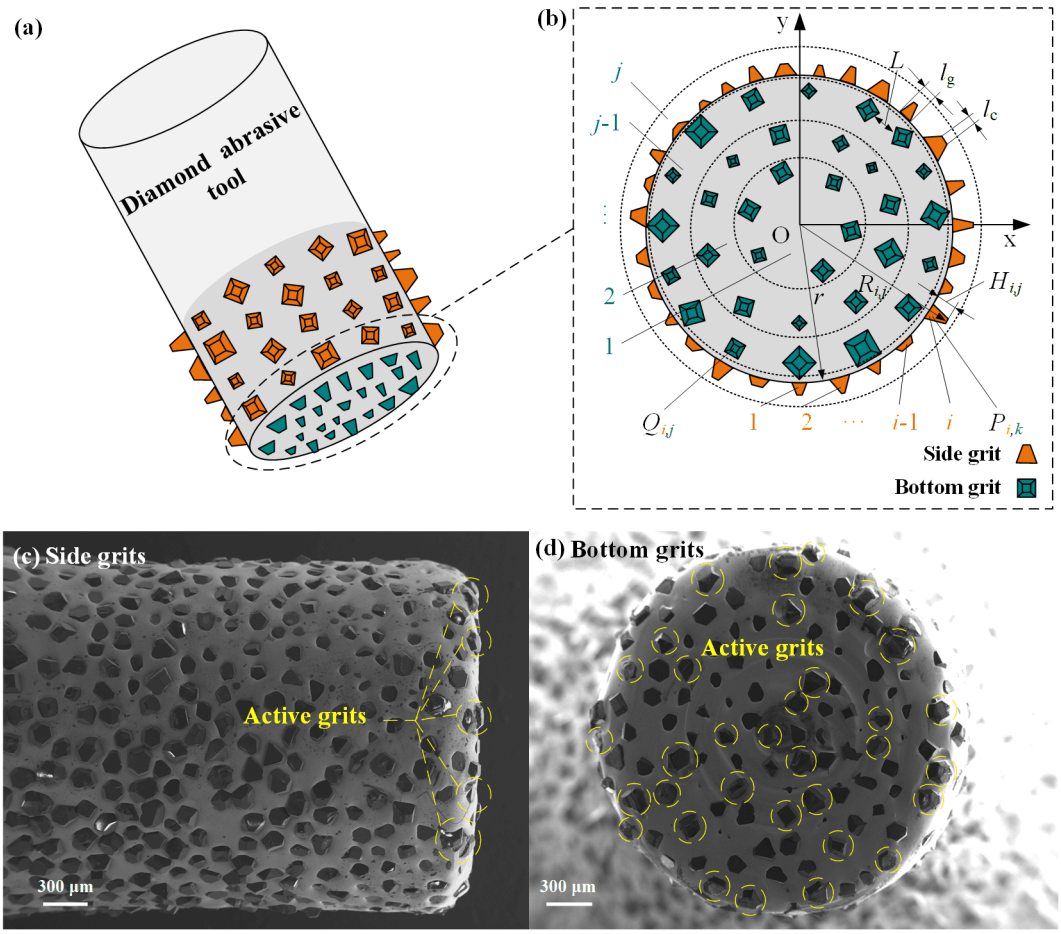

Fig.2. Geometric distribution of side and bottom diamond abrasive grits on the tool (a) the whole tool (b) the 1 to j element (c) side grits of worn tool (d) bottom grits of worn tool

The dynamic radius of the i^{th} grit in j^{th} element can be expressed as

$$R_{i,j} = r + H_{i,j} \tag{1}$$

During UVHG process, the tool's motion is shown in **Fig.3a**. The tool with a radius of r rotates around its axis at a speed of n_s while revolving around the center of the hole at a speed of n_r with an eccentric distance of r'. Simultaneously, the tool undergoes axial feed motion, resulting in a reduction of cutting depth by a_p for each complete revolution. v_s and v_r are the linear velocities of tool rotation and revolution, respectively.

$$v_s = \frac{n_s \pi r_{i,j}}{30} \tag{2}$$

$$v_r = \frac{n_r \pi r'}{30} \tag{3}$$

f_r, f_s and f_a are the feed rate of the tool along the helical line, horizontal feed rate, and axial feed rate, respectively. ζ is the angel between the horizontal feed rate of grits and the resultant speed. As the spindle speed during UVHG is in the range of 10,000 to 20,000 r/min (approximately 78,539–157,079 mm/min in this study), but the feed rate is only 50–200 mm/min, the horizontal feed rate is relatively small.

$$\tan\zeta = \frac{f_a}{f_s} = \frac{a_p}{2\pi r_{i,j}} \tag{4}$$

$$f_a = f_r \cdot \sin\zeta = \frac{a_p n_r}{60} \tag{5}$$

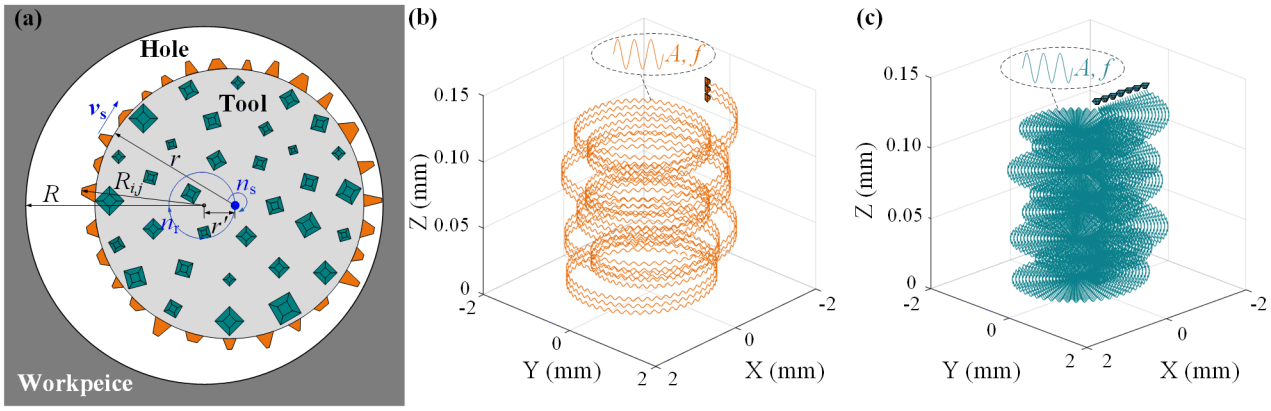

Fig.3 Tool motion in UVHG (a) tool movement in hole grinding; (b) trajectory of side grit; (c) trajectory of bottom grit

The trajectory of each cutting edge on side diamond abrasive grits for the i^{th} grit in j^{th} element can be expressed as

$$x_{i,k} = (r + H_{i,j}) \cdot \cos\left(\frac{2\pi n_s}{60} t\right) + r' \cos\left(\frac{2\pi n_r}{60} t\right) \tag{6}$$

$$y_{i,k} = (r + H_{i,j}) \cdot \sin\left(\frac{2\pi n_s}{60} t\right) + r' \sin\left(\frac{2\pi n_r}{60} t\right) \tag{7}$$

$$z_{i,k} = v_r t + A \sin 2\pi f t \tag{8}$$

The trajectory of each cutting edge on bottom diamond abrasive grits for the i^{th} grit in j^{th} element

can be expressed as

$$x_{i,j} = r_{i,j}\cos\left(\frac{2\pi n_s}{60}t\right) + r'\cos\left(\frac{2\pi n_r}{60}t\right) \tag{9}$$

$$y_{i,j} = r_{i,j}\sin\left(\frac{2\pi n_s}{60}t\right) + r'\sin\left(\frac{2\pi n_r}{60}t\right) \tag{10}$$

$$z_{i,j} = v_r t + A\sin 2\pi ft \tag{11}$$

The schematic diagrams of **Fig.3b** and **Fig.3c** illustrate the motion trajectories of the side abrasive grits and bottom abrasive grits, respectively. During UVHG process, the grinding is primarily carried out by the abrasive grits at the bottom of the tool, while the quantity of abrasive grits on the side participating in the grinding process is mainly influenced by the axial feed depth per helical revolution. According to the theory of Budak et al, the grit is considered "active" if its path intersects with the path of the previous active grit. Hence, the determination of active grits can be achieved by assessing the static number of grits, grits spacing, grits height and grits width distribution of abrasive grits on the tool. Specifically, employing relevant formulas, the motion trajectories of the i^{th} and i+1th grits can be computed, enabling the identification of active grits.

2.2 Undeformed chip thickness and cross-sectional area of a single grit

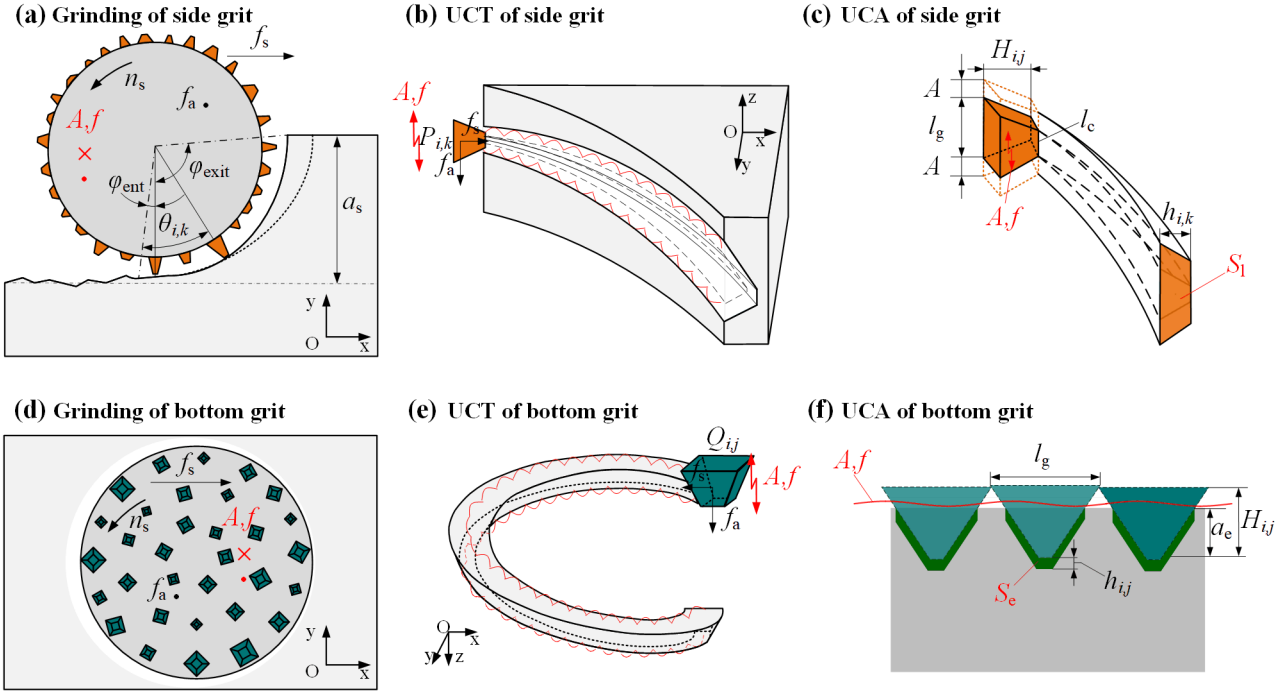

Fig.4. Chip formation process in grinding zone (a) side grit-workpiece interaction (b) undeformed chip thickness of side grit (c) undeformed chip cross-sectional area of side grit (d) bottom grit-workpiece interaction (e) undeformed chip thickness of bottom grit (f) undeformed chip cross-sectional area of bottom grit

During the UVHG process, the chip formation process in grinding zone is shown in **Fig.4**. For the side grit, the direction of ultrasonic vibration is perpendicular to the horizontal feed direction of the abrasive grits (**Fig.4a**). Consequently, the vibration increases the contact length and area with the composites(**Fig.4b**). The instantaneous undeformed chip thickness of the side grit can be expressed as follows,

$$h_{i,k}\left(\theta_{i,k}\right)=R_{n,k}-R_{m,k}+\left(n-m\right)\cdot f_{\mathrm{s}}\sin\left(\theta_{i,k}\right),\varphi_{\mathrm{ent}}<\theta_{i,k}<\varphi_{\mathrm{exit}} \tag{12}$$

where $R_{\mathrm{r,n}}$ and $R_{\mathrm{r,m}}$ are the radius of two adjacent active grits (the n^{th} and m^{th} side grit), f_{s} is the horizontal feed rate of side grit, $\theta_{i,k}$ is immersion angle of the grit varying from φ_{ent} to φ_{exit}. a_{s} is the cutting depth of side grits.

$$\varphi_{\mathrm{ent}}=\sin^{-1}\left(\frac{R_m-R_n}{(n-m)f_{\mathrm{s}}}\right) \tag{13}$$

$$\varphi_{\mathrm{exit}}=\cos^{-1}\left(1-\frac{a_{\mathrm{s}}-R_{\max}+R_n}{R_n}\right) \tag{14}$$

As the movement of the side grits is perpendicular to the direction of ultrasonic vibration. From the perspective of kinematic analysis, the instantaneous cross-sectional area of undeformed chip tends to increase compared to conventional machining (**Fig.4c)**. Thus, the UCA of side grit S_{l} can be calculated as follows:

$$S_{\mathrm{l}}=\left[l_{\mathrm{c}}+\frac{h_{i,k}(l_{\mathrm{g}}-l_{\mathrm{c}})}{2H_{i,j}}+2A\right]h_{i,k} \tag{15}$$

For the bottom grit, the undeformed chip thickness of a single grit is equal to the axial feed depth after one revolution of self-rotation. As the direction of ultrasonic vibration is parallel to the axial feed direction of the abrasive grits (**Fig.4d)**. Thus, the vibration change the contact length and area of the grits with the composites(**Fig.4e)**. Under the high frequency of ultrasonic vibration, the rotational speed of girts is relatively slower in comparison to the velocity of the vibration. Consequently, The instantaneous undeformed chip thickness of the bottom grit can be expressed as follows,

$$h_{i,j}=\frac{60f_a}{n_{\mathrm{s}}N_{\mathrm{b}}}+2A \tag{16}$$

where N_{b} is the number of active bottom grits involve in grinding.

As the motion induced by ultrasonic vibration is smaller than that of feed motion, the ultrasonic vibration expands the undeformed chip cross-sectional area of bottom grits as shown in **Fig.4f**. Thus, the UCA of bottom grits S_{e} can be calculated as follows:

$$S_{\mathrm{e}}=\left[l_{\mathrm{c}}+\frac{\left(l_{\mathrm{g}}-l_{\mathrm{c}}\right)a_{\mathrm{e}}}{H_{i,j}}\right]h_{i,j} \tag{17}$$

where a_{e} is the cutting depth of bottom grits, $a_{\mathrm{e}}=a_{\mathrm{p}}-a_{\mathrm{s}}$.

2.3 Composition of the grinding force of a single grit

Given the material removal mechanism and ultrasonic vibration characteristics, plastic deformation of aluminum alloy matrix and brittle fracture of SiC particles are the primary material removal forms during the grinding process. Thus, the UVHG force of SiC_p/Al composites can be divided into kinds of force under different removal forms.

The UVHG force $\boldsymbol{F}$ consists of two parts: side grinding force $\boldsymbol{F}_{\mathrm{SG}}$ and end grinding force $\boldsymbol{F}_{\mathrm{EG}}$. For the side grinding part, the side grinding force can be divided into the plastic deformation force of aluminum alloy matrix $\boldsymbol{f}_{\mathrm{SGP}}$, fracture force of SiC particles $\boldsymbol{f}_{\mathrm{SGF}}$, and friction force $\boldsymbol{f}_{\mathrm{SGf}}$. For the end grinding part, the grinding force can also be divided into the plastic deformation force $\boldsymbol{f}_{\mathrm{EGP}}$, fracture force $\boldsymbol{f}_{\mathrm{EGF}}$, and friction force $\boldsymbol{f}_{\mathrm{EGf}}$. Therefore, the composition of grinding force $\boldsymbol{F}$ can be expressed as

follows:

$$\begin{cases} \boldsymbol{F} = \boldsymbol{F}_{\mathrm{SG}} + \boldsymbol{F}_{\mathrm{EG}} \\ \boldsymbol{F}_{\mathrm{SG}} = \boldsymbol{f}_{\mathrm{SGP}} + \boldsymbol{f}_{\mathrm{SGF}} + \boldsymbol{f}_{\mathrm{SGf}} \\ \boldsymbol{F}_{\mathrm{EG}} = \boldsymbol{f}_{\mathrm{EGP}} + \boldsymbol{f}_{\mathrm{EGF}} + \boldsymbol{f}_{\mathrm{EGf}} \end{cases} \tag{18}$$

2.3.1 Plastic deformation force of matrix

Whether it is assisted by ultrasonic vibration, the aluminum alloy matrix is plastically deformed under the grinding of diamond grits. But the addition of scattered SiC particles eliminates the flowability of the matrix material, which enhances the strength of the matrix. To simplify the calculation, the SiC_p/Al composites are considered equivalent homogeneous materials (EHM). The diamond grits contact the material continuously in the side grinding process, and the plastic deformation force can be calculated as the contact stress σ_{m} times the contact area. According to the literature [50], the contact stress between a single grit and workpiece material can be equal to the yield limit σ_{s} of the SiC_p/Al composites when the average UCT is less than 6.87 μm:

$$\sigma_m = \sigma_s \tag{19}$$

Our previous research has confirmed the occurrence of the "acoustic softening" phenomenon in SiC_p/Al composites under ultrasonic vibration, resulting in a reduction in compressive strength. The mechanism can be attributed to the instantaneous high strain rate induced by ultrasonic vibration, which promotes the movement of dislocations within the aluminum matrix. As a result, dislocations are more prone to annihilation, leading to a decrease in the dislocation density within the aluminum matrix and a reduction in the composites' deformation stress. Consequently, the softening coefficient ψ is defined to correct the yield strength caused by ultrasonic vibration, considering ultrasonic vibration's "acoustic softening" effect [41,42,43,44].

The schematic diagram of plastic deformation force exerted by side grits is shown in **Fig.5a**. According to the literature[39], the tangential and normal forces acting on the contact area can be expressed as:

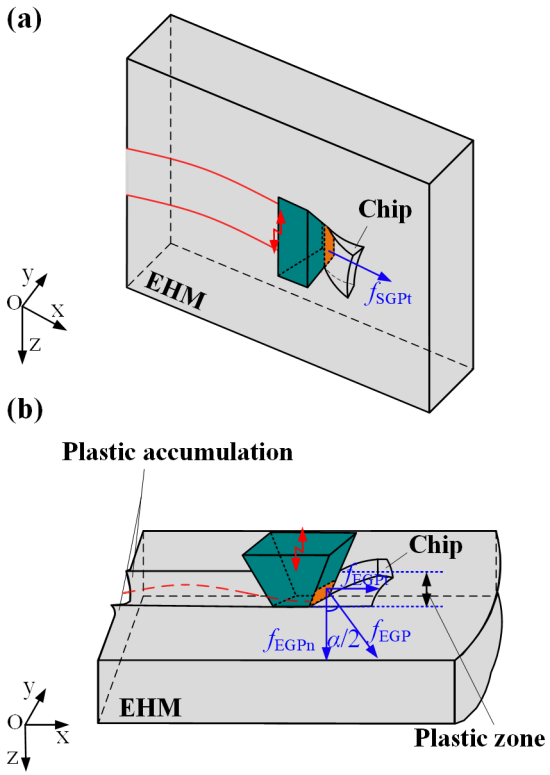

Fig.5. Plastic deformation force of (a) side grit; (b) bottom grit

$$\begin{cases} f_{\mathrm{SGPn}} = 0 \\ f_{\mathrm{SGPt}} = \psi \sigma_{\mathrm{m}} S_{\mathrm{l}} \end{cases} \tag{20}$$

For the bottom grits, the plastic deformation force should be equal to the contact stress multiplied by the contact area at any moment, as shown in **Fig.5b**. To simplify the calculation, the instantaneous plastic deformation force is represented by the average force in one ultrasonic vibration cycle. The tangential and normal forces acting on the contact area can be expressed as:

$$\begin{cases} f_{\mathrm{EGPn}} = \psi \sigma_{\mathrm{m}} S_{\mathrm{e}} \cos \dfrac{\alpha}{2} \\ f_{\mathrm{EGPt}} = \psi \sigma_{\mathrm{m}} S_{\mathrm{e}} \sin \dfrac{\alpha}{2} \end{cases} \tag{21}$$

2.3.2 Particle fracture force

During UVHG of SiC_p/Al, the SiC particles come into contact with the bottom and side of the cutting tool. The particles on the bottom are mainly compressed, and the particles on the side are mainly sheared by the diamond grits on the tool.

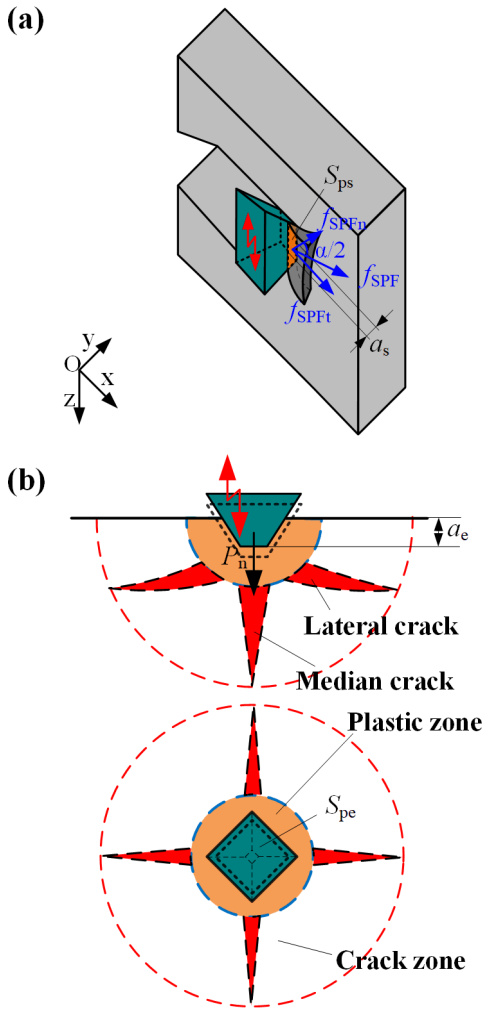

Fig.6. Particle fracture force of (a)side grit; (b) bottom grit

For the particles on the side, previous research [51] has shown that tensile stress is the main factor leading to SiC particles' fracture during the processing of SiC_p/Al. According to the modified Griffith's theory [52], the tensile stress of SiC particle can be expressed as:

$$\sigma_p = \sqrt{\frac{E\left(2\gamma_{se}+\gamma_{pw}\right)}{\pi L\left(1-\nu^2\right)}} \tag{22}$$

Where σ_p is the fracture stress, γ_{se} is the surface energy when particles fracture, γ_{pw} is the plastic work required for crack propagation per unit area, and L is the material constant and represents the crack length under static load. Usually, the fracture surface energy γ_s of SiC can be calculated as half of the energy release rate G_c (strain energy) for crack formation, which is:

$$G_c = \frac{K_{IC}^2}{E} = 2\gamma_{se}+\gamma_{pw} \tag{23}$$

Thus,

$$\sigma_p = \sqrt{\frac{K_{IC}^2}{\pi L\left(1-\nu^2\right)}} \tag{24}$$

In the side grinding process (**Fig.6a**), the contact area between fracture particles and diamond grits can be approximately equal to the average contact area between diamond grits and material at a specific cutting depth multiplied by the volume fraction of SiC particle:

$$S_{\mathrm{ps}} = \omega_{\mathrm{SiC}} \left(\frac{a_{\mathrm{s}}^2 \left(l_{\mathrm{g}} - l_{\mathrm{c}} \right)}{2H_{i,j}} + l_{\mathrm{c}} a_{\mathrm{s}} \right) \tag{25}$$

Therefore, the tangential and normal force of particle removal f_{SPFt} and f_{SPFn} are respectively expressed as follows:

$$\begin{cases} f_{\mathrm{SPFn}} = 0 \\ f_{\mathrm{SPFt}} = \sigma_{\mathrm{p}} \cdot S_{\mathrm{ps}} = \omega_{\mathrm{SiC}} \left(\dfrac{a_{\mathrm{s}}^2 \left(l_{\mathrm{g}} - l_{\mathrm{c}} \right)}{2H_{i,j}} + l_{\mathrm{c}} a_{\mathrm{s}} \right) \sqrt{\dfrac{\mathrm{K}_{\mathrm{IC}}^2}{\pi L \left(1 - \nu^2 \right)}} \end{cases} \tag{26}$$

For the particles on the bottom, the crack initiation is caused by diamond grits, as shown in **Fig.6b**. According to indentation fracture mechanics of SiC, the critical load leading to crack generation can be expressed as:

$$P_{\mathrm{n}} = \left(54.47\kappa / \xi^2 \zeta^4 \right) \left(\mathrm{K}_{\mathrm{IC}} / \mathrm{H}_{\mathrm{V}} \right)^2 \mathrm{K}_{\mathrm{IC}} \tag{27}$$

where κ=2π for the pyramidic grits in the research; ξ and ζ are also dimensionless constants, ξ=0.1, ζ=0.2 in the study [53].

The fracture force of the SiC particle on the bottom face should equal the sum of the forces between all active diamond grits and the broken SiC particle. Given the perpendicular vibration of bottom grits, the action area of diamond grits on the SiC particle can be similar to the average contact area between diamond grits and the SiC particle during vibration. Thus, the action area of the SiC particle S_{pe} can be calculated as follows:

$$S_{\mathrm{pe}} = 2a_{\mathrm{s}} l_{\mathrm{c}} + \frac{2a_{\mathrm{s}}^2 \left(l_{\mathrm{g}} - l_{\mathrm{c}} \right)}{H_{i,j}} + l_{\mathrm{c}}^2 \tag{28}$$

According to K. Tohgo's [54] research, the volume fraction of the damaged particle is nearly equal to the volume fraction of the particle in whole composites. Thus, the particle fracture force of the bottom grits can be expressed as follows:

$$\begin{cases} f_{\mathrm{EPFn}} = \omega_{\mathrm{SiC}} S_{\mathrm{pe}} P_{\mathrm{n}} \cos \dfrac{\alpha}{2} \\ f_{\mathrm{EPFt}} = \omega_{\mathrm{SiC}} S_{\mathrm{pe}} P_{\mathrm{n}} \sin \dfrac{\alpha}{2} \end{cases} \tag{29}$$

where ω_{SiC} is the volume fraction of the SiC particle.

2.3.3 Friction force

In the UVHG process, the friction force mainly comes from the interaction between the diamond grits and the chips, the worn diamond grits, and the machined surface [55]. To simplify the calculation, the fracture of SiC particles is neglected during friction, and only sliding friction between the diamond grit and the SiC_p/Al composites is considered in this model. Previous research illustrated the validity of Coulomb's friction law even for ultrasonic conditions [56]. Therefore, the sliding force is calculated by Coulomb's law.

The diamond grit continuously slides on the surface for the side grinding process. The coefficient of friction μ_{s} can be considered a fixed value.

Thus, the normal and tangential frictional force of side grits can be expressed as follows:

$$\begin{cases} f_{\mathrm{SGfn}} = 0 \\ f_{\mathrm{SGft}} = \mu_{\mathrm{s}}\sigma_{\mathrm{s}}S_{\mathrm{l}} \end{cases} \tag{30}$$

The diamond grit slides on the sample surface for the end grinding process of SiC_p/Al. The average coefficient of friction is μ_e in the end grinding process. Thus, the normal and tangential frictional force of bottom grits can be expressed as follows:

$$\begin{cases} f_{\mathrm{EGfn}} = \mu_{\mathrm{e}}\sigma_{\mathrm{s}}S_{\mathrm{e}}\cos\dfrac{\alpha}{2} \\ f_{\mathrm{EGft}} = \mu_{\mathrm{e}}\sigma_{\mathrm{s}}S_{\mathrm{e}}\sin\dfrac{\alpha}{2} \end{cases} \tag{31}$$

2.4 Total grinding force

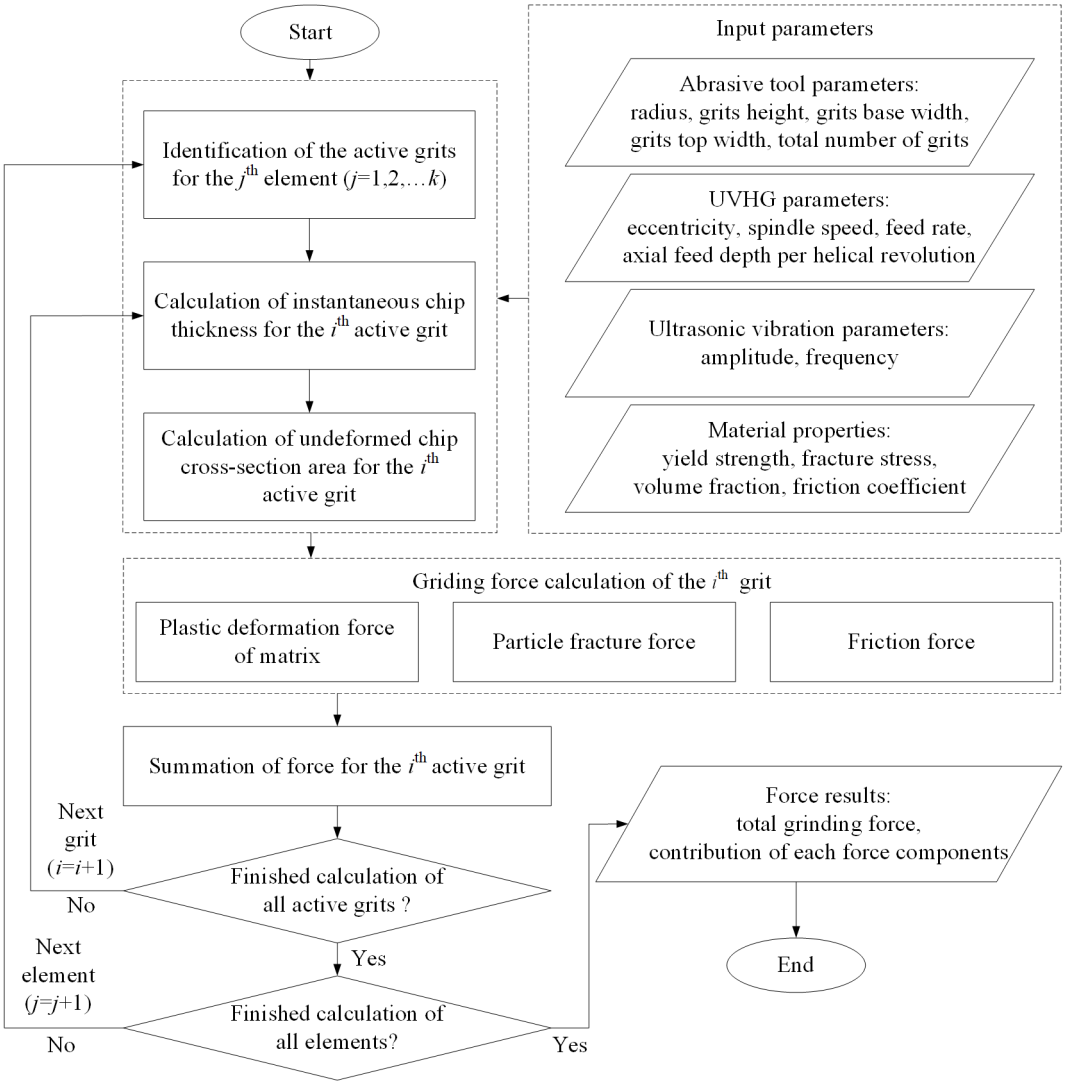

Fig.7. Algorithm of the UVHG force model

As mentioned in section 2.3, the normal and tangential grinding force of a single grit can be expressed as follows:

$$\begin{cases} \boldsymbol{F}_{ij} = \boldsymbol{F}_{\mathrm{n}(i,j)} + \boldsymbol{F}_{\mathrm{t}(i,j)} \\ F_{\mathrm{n}(i,j)} = f_{\mathrm{SGPn}} + f_{\mathrm{SPFn}} + f_{\mathrm{SGfn}} + f_{\mathrm{EGPn}} + f_{\mathrm{EPFn}} + f_{\mathrm{EGfn}} \\ F_{\mathrm{t}(i,j)} = f_{\mathrm{SGPt}} + f_{\mathrm{SPFt}} + f_{\mathrm{SGft}} + f_{\mathrm{EGPt}} + f_{\mathrm{EPFt}} + f_{\mathrm{EGft}} \end{cases} \tag{32}$$

substitute Eq.(17), (18), (23), (26)–(28) into Eq.(29),

$$\begin{cases} F_{\mathrm{n}(i,j)} = \psi\sigma_{\mathrm{m}} S_{\mathrm{e}} \cos\dfrac{\alpha}{2} + \omega_{\mathrm{SiC}} S_{\mathrm{pe}} P_{\mathrm{n}} \cos\dfrac{\alpha}{2} + \mu_{\mathrm{e}}\sigma_{\mathrm{s}} S_{\mathrm{e}} \cos\dfrac{\alpha}{2} \\ F_{\mathrm{t}(i,j)} = \psi\sigma_{\mathrm{m}} S_{\mathrm{l}} + \omega_{\mathrm{SiC}} \left(\dfrac{a_{\mathrm{s}}^2 \left(l_{\mathrm{g}} - l_{\mathrm{c}}\right)}{2H_{i,j}} + l_{\mathrm{c}} a_{\mathrm{s}} \right) \sqrt{\dfrac{\mathrm{K}_{\mathrm{IC}}^2}{\pi L\left(1-\nu^2\right)}} + \mu_{\mathrm{s}}\sigma_{\mathrm{s}} S_{\mathrm{l}} \\ \qquad + \psi\sigma_{\mathrm{m}} S_{\mathrm{e}} \sin\dfrac{\alpha}{2} + \omega_{\mathrm{SiC}} S_{\mathrm{pe}} P_{\mathrm{n}} \sin\dfrac{\alpha}{2} + \mu_{\mathrm{e}}\sigma_{\mathrm{s}} S_{\mathrm{e}} \sin\dfrac{\alpha}{2} \end{cases} \tag{33}$$

The total grinding force of the UVHG process is obtained by summing the individual grinding forces exerted by each active grit on every element. The algorithm of calculating the UVHG force is shown in **Fig.7**.

$$\begin{cases} F_{\mathrm{n\_total}} = \sum_{j=1}^{k} \sum_{i=1}^{m} F_{\mathrm{n}(i,j)} \\ F_{\mathrm{t\_total}} = \sum_{j=1}^{k} \sum_{i=1}^{m} F_{\mathrm{t}(i,j)} \end{cases} \tag{34}$$

where m is the total number of active grits in j^{th} element.

3. The validation of the force model

3.1 Determination of model parameters

3.1.1 Ultrasonic softening coefficient

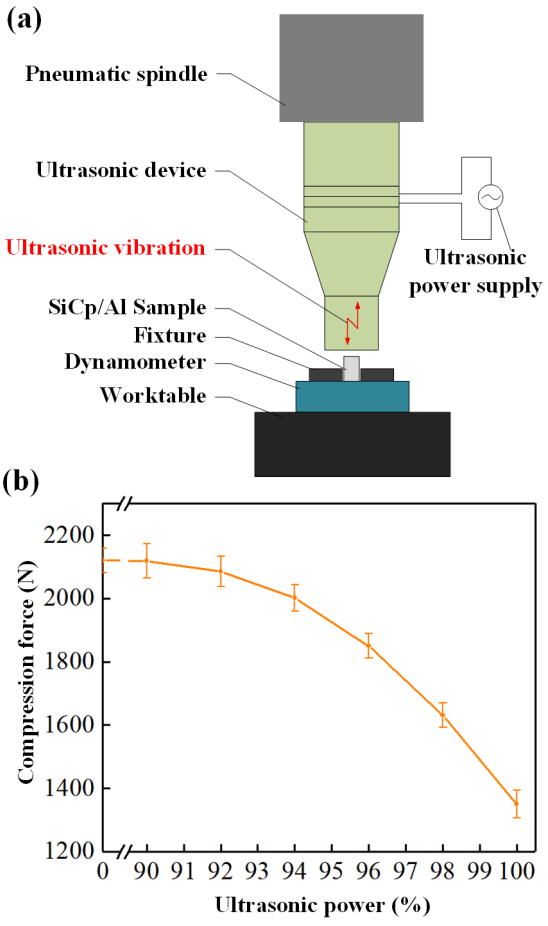

Fig.8. Ultrasonic softening coefficient test: (a) experimental setup of ultrasonic compression test, (b) compression force of SiC_p/Al composites under various ultrasonic power

The SiC_p/Al composites in this research are manufactured by powder metallurgy and hot isostatic pressing. The main properties are listed in **Table 1**.

Table 1 Properties of SiC_p/Al composites

Properties	Value
Average size of SiC particles (μm)	7.0
Volume fraction of SiC (%)	45.0
Thermal conductivity ($W \cdot mK^{-1}$, 373.15K)	160.0
Passion ratio	0.3
Coefficient of thermal expansion ($10^{-6} \cdot K^{-1}$)	9.5

Considering the 'acoustic softening' effect of SiC_p/Al composites due to the reduction of compressive strength and flow stress by ultrasonic vibration, an ultrasonic vibration compression test is designed and carried out to obtain the softening of the material under vibration [57]. A standard 2 mm diameter by 2 mm high cylindrical specimen was mounted on a force-measuring instrument. The ultrasonic vibration compression device is mounted on a pneumatic spindle, and the spindle can adjust the compression speed and height. The ultrasonic compression device mainly comprises a piezoelectric ultrasonic transducer driven by a unique ultrasonic power supply. The power supply power can be adjusted as shown in **Fig.8a**. During the test, a compression rate of $1 \times 10^{-3} m \cdot s^{-1}$ was used to compress the specimen, while the maximum compression load of the sample is compressed to 50% of the deformation was recorded by a dynamometer. The compression load under different ultrasonic parameters was recorded by changing the ultrasonic power supply power, and each group of tests was repeated five times.

Fig.8b shows that the compression force of SiC_p/Al composites gradually becomes smaller as the ultrasonic power increases, which increases the ultrasonic vibration amplitude. When the ultrasonic power is lower than 90%, the compressive force of SiC_p/Al composites is 2085N, which means the compressive stress is 664.01MPa. When the ultrasonic power is 100%, the compressive force is only 1350N, which means the compressive stress is 429.94MPa. In comparison, it is reduced by 35.25%. That is, when the ultrasonic vibration works on the SiC_p/Al composites, it produces a specific softening effect on the material and reduces the compressive stress of the material. Therefore, in this paper's model and the cutting test, the ultrasonic power was set to 100%, and the softening coefficient ψ of ultrasonic vibration was set as 0.3525.

3.1.2 Friction coefficient

Frictional force is an indispensable and crucial factor in the UVHG process, and modeling the frictional forces in ultrasonic vibration-assisted machining is a highly challenging task【】. Jamshidi et al. developed a frictional model of ultrasonic-vibration-assisted turning by considering the tool-chip contact【】. Yongjie Bao et al. studied the friction force between diamond and SiC_p/Al composites [39]. But the friction force of UVHG of SiC_p/Al composites has not been reported. To improve the modeling accuracy and the model's engineering applicability , the binomial law of friction is used to characterize the coefficient of friction (COF) in this model. The friction coefficients of bottom grit μ_e and side grit μ_s can be expressed as

$$\mu_e = \mu_1 + k_1 v_s \tag{35}$$

$$\mu_s = \mu_2 + k_2 v_s \tag{36}$$

where μ_1 and μ_2 are the coefficients of bottom grit and side grit at relatively low speed (0.5mm·min^{-1}), k_1 and k_2 are the constant to modify the friction coefficient at various cutting speeds, which need to be obtained through experiments.

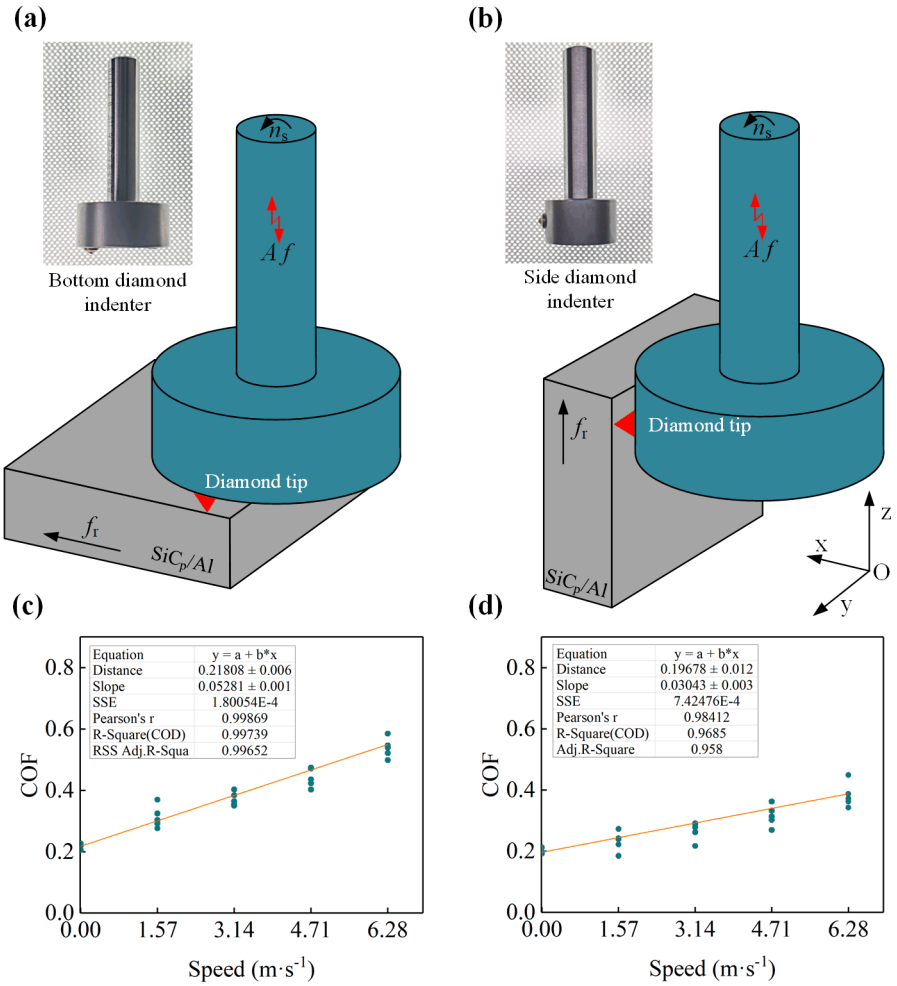

Fig.9. Friction coefficient test: (a)ultrasonic scratch test of bottom diamond indenter; (b) ultrasonic scratch test of side diamond indenter; (c) the coefficient of bottom grit at various scratch speed; (d) the coefficient of side grit at various scratch speed;

The ultrasonic vibration-assisted scratch tests under various speed are conducted to obtain the coefficient of friction (COF)【 】, and the test schematic is shown in **Fig.9a&b**. Longitudinal vibration is applied to the customized bottom and side diamond indenter to scratch the polished SiC_p/Al surface to simulate the process of grinding the material. The frequency and amplitude of vibration is 20kHz and 5μm, respectively. The diamond indenter exhibits a rounded tip characterized by a circular arc with a radius of 150μm. The apex angle measures 136 degrees, and it is situated at a radial distance of 10mm from the center of rotation. The scratch parameters are shown in **Table 2**, and each experiment was repeated five times. The dynamometer of Kistler 9257b is used to record the average scratching force.

Table 2 Experimental parameters for ultrasonic vibration-assisted scratching

Spindle speed (rpm)	Feed rate (mm·min^{-1})	Scratch depth (μm)
0,1500,3000,4500,6000	0.5	5

According to Coulomb's law, the friction force during scratching can be approximated as a tangential force than a normal force. Thus, the coefficient of friction can be expressed as

$$\mu = \frac{F_t}{F_n} \tag{37}$$

By analyzing the scratch force in the scratch process and calculating the coefficient of friction according to Eq.(34), the friction coefficients of bottom grits and side grits under different scratch speed are obtained, as shown in **Fig.9c&d**. Thus, The friction coefficients of bottom grit μ_e and side grit μ_s can be expressed as

$$\mu_e = 0.2180 + 0.0528 v_s \tag{38}$$

$$\mu_s = 0.1968 + 0.0304 v_s \tag{39}$$

3.1.3 Characterization of diamond abrasive tools

In this modeling, the electroplated diamond abrasive tools are used. **Fig.10a&b** illustrates the distribution of bottom abrasive grits and side abrasive grits. The characteristic parameters of abrasive grains are measured and analyzed using confocal microscopy (**Fig.10c&d**). More than 100 grits' properties are obtained through the microscope (DSX1000, Olympus Inc., Japan) and the results are statistically listed in in **Table 3**. As shown in **Fig.10e&f,** the mean exposure height of abrasive grains is 54.09 μm, with a standard deviation of 23.39 μm. The mean width of cut is 89.11 μm, with a standard deviation of 33.86 μm.

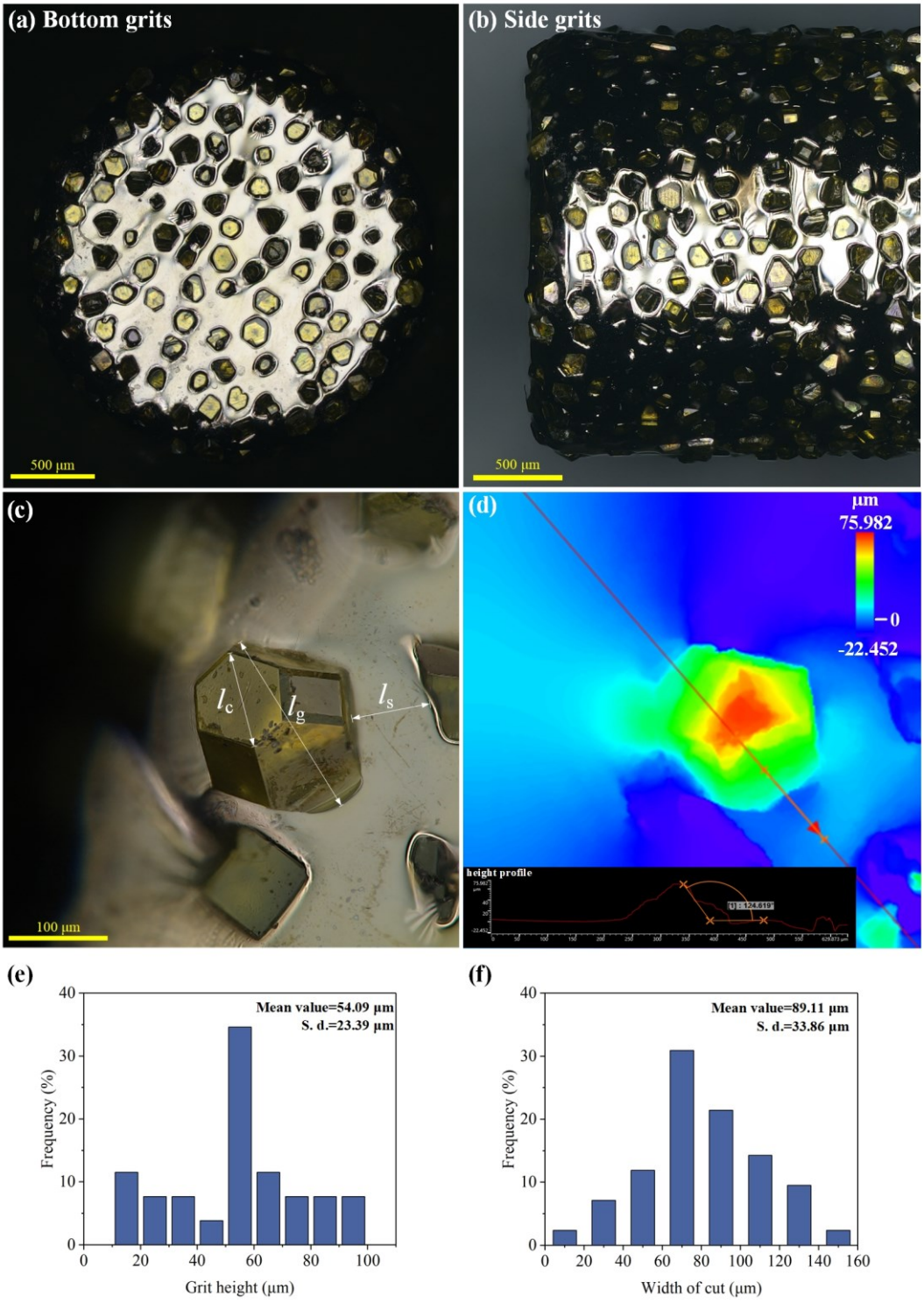

Fig.10. Diamond abrasive grits on the tool: (a) bottom grits; (b) side grits; (c) geometric parameters of exposed grit; (d) height profile of exposed grit

Table 3 Characterization of diamond abrasive tool

Tool type	#100
Diameter (mm)	2.5
Static number of bottom grits	100
Static number of side grits (at 0.5mm height range)	90
Mean value of grit spacing (μm)	81.77
Mean value of grit width (μm)	131.56
Mean rake angle of grit (°)	70.82
Mean and standard deviation of girts height (μm)	54.09 & 23.39
Mean and standard deviation of width of cuts (μm)	89.11 & 33.86

3.2 Model validation test settings

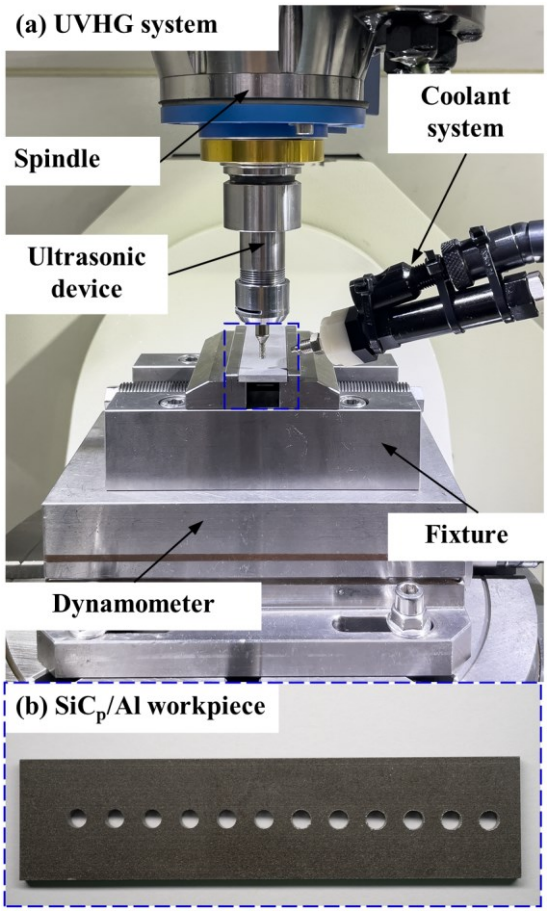

Fig.11. Experimental setup: (a)UVHG system (b) SiC_p/Al sample

The model verification experiments were conducted on the five-axis high-speed machine tool Beijing Jingdiao JD200. The maximum spindle speed of the machine tool was 32000rpm, as shown in **Fig.11a**. The X, Y, and Z axis positioning accuracy of the machine tool is 6μm, and repeated positioning accuracy is 5μm. The ultrasonic vibration device has a frequency of 20kHz and an amplitude of 5μm. The output power was set to 100%. A #100 tool with a diameter of 2.5mm is used to grind through holes. The SiC_p/Al sample used in the experiments is cut into a rectangular parallelepiped plate with a thickness of 3mm in advance **(Fig.11c)**. To ensure the success of grinding and avoid defects such as edge chipping during processing, the experimental parameters are listed in **Table 4**.

Table 4 Parameters of model verification experiment

Spindle speed (rpm)	Feed rate ($mm \cdot min^{-1}$)	axial feed depth per helical revolution (mm)
11000,14000,17000,20000,23000	100	0.05
17000	80,120,140,160	0.05
17000	100	0.04,0.06,0.07,0.08

3.3 Results and discussions

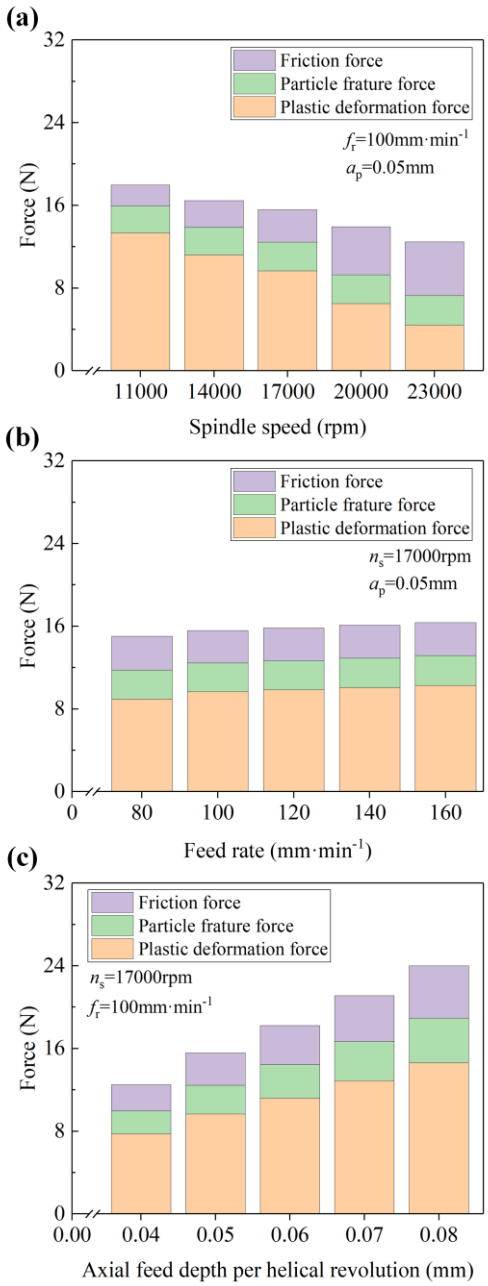

Fig.12 Compositions of the predicted grinding forces under the experimental parameters

Fig.12 displays the predicted grinding forces and their detailed compositions under the experimental conditions based on the established model. It can be seen that within the experimental parameter range, the total grinding force decreases with increasing spindle speed when feed rate and axial feed depth per helical revolution are constant **(Fig. 12a**). Among the components, the plastic deformation force and friction force changemore notably compared to particle fracture force. Specifically, the plastic deformation force gradually decreased while the friction force increased with rising spindle speed. This could be attributed to the variation in undeformed chip thickness of the abrasive grits at the tool bottom (Eq. 16). Moreover, as the spindle speed goes up, the arc length of grain-workpiece contact per unit time is enlarged, which is likely one of the reasons for the growth of friction force. When spindle speed and axial feed depth per helical revolution are fixed, although the total grinding force increases with feed rate (**Fig. 12b**), the increasing tendency is gentle within the experimental parameter range. The reasons can be summarized as that the horizontal feed has little influence on undeformed chip thickness and cross-sectional area. Also, the axial feed component

can be ignored due to the small feed angle (1°-3°) of the tool; thus, the variation of feed rate does not significantly impact the predicted grinding force from the model. Another possible reason is that the selected feed rate range in the experiments is not wide enough for remarkable change. (Typical processing parameters are chosen considering machining time and efficiency in this study.) The changing trends of individual force components also exhibit slow growth. With fixed spindle speed and feed rate, the predicted grinding force by the model markedly increases with larger axial feed depth per helical revolution (**Fig. 12c**). Herein, the forces stemming from plastic deformation, particle fracture, and friction all rise substantially. This is because both the undeformed thickness and cross-sectional area increase with greater axial feed depth per helical revolution, leading to intensified resistance in material removal. Furthermore, the compositions signify that plastic deformation force takes up most of the grinding force, while the friction force accounts for a considerable proportion when the spindle speed reached 23,000 rpm.

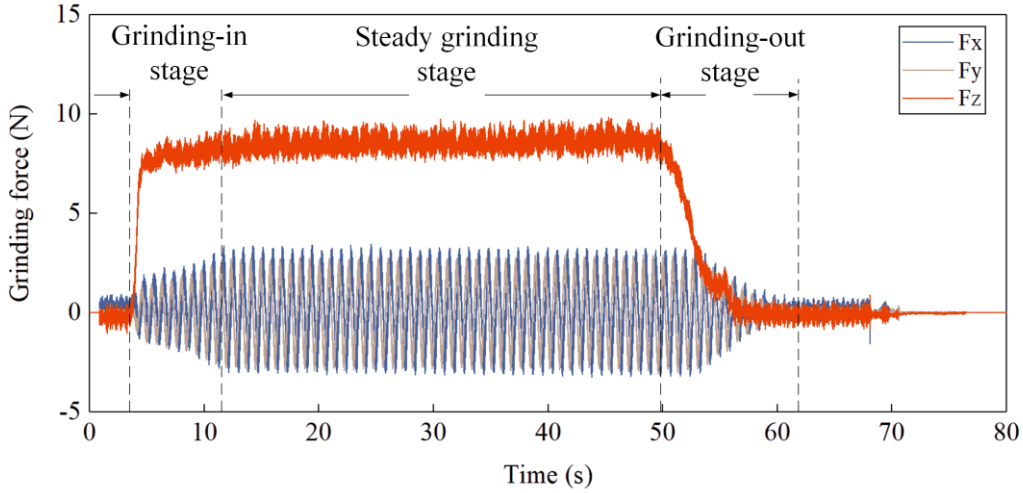

Fig.13. Grinding force characteristics of UVHG (n_s=23000rpm, f_r=110 mm·min^{-1}, a_p=0.05mm)

To further understand the variation of grinding forces, the grinding force characteristics obtained by dynometer during UVHG are shown in **Fig.13**. According to the change of grinding force, it can be divided into three stages, the grinding-in stage, the steady grinding stage, and the grinding-out stage. During the whole grinding process, the axial force is the main cutting force, and the grinding force increases rapidly in the axial direction (F_z) when the tool contacts the workpiece surface along the axial direction as the bottom grits start to remove the material. Due to the helical feed mode, the radial (F_x, F_y) force increases slowly, and the tool moves reciprocally in the radial plane. Hence, the radial force shows positive and negative changes. In this modeling work, the radial grinding force was taken as the absolute value, and only the average value in the stable grinding stage was considered.

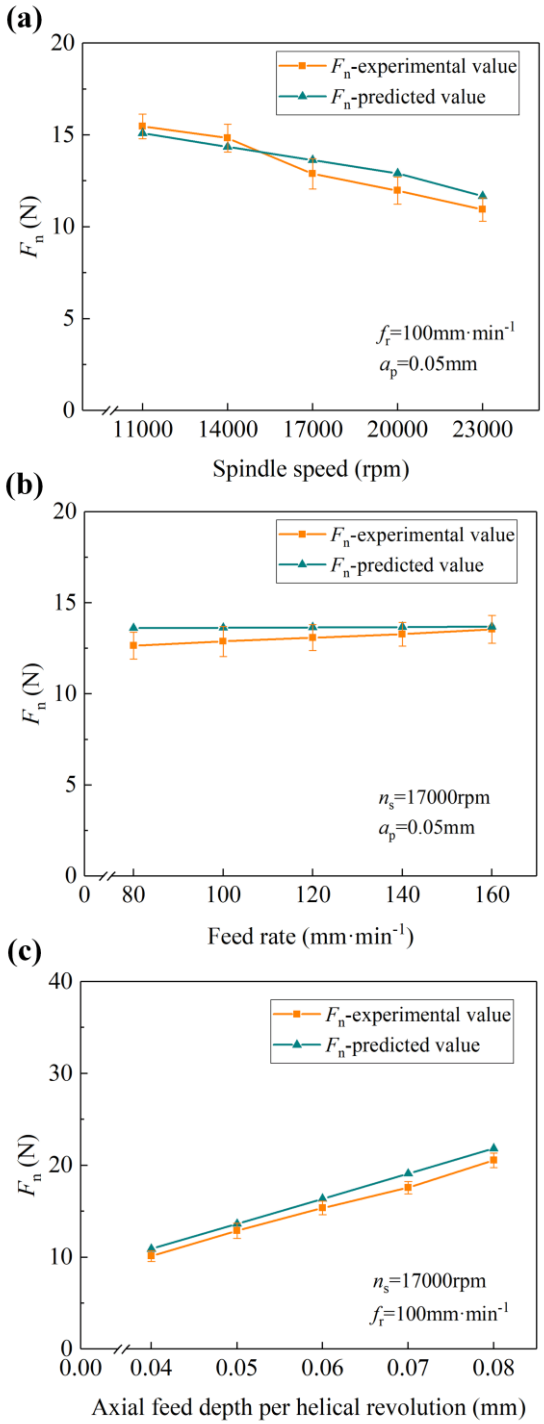

Fig.14. Experimental and predicted normal grinding force under the experimental parameters

The predicted and experimental values of the normal grinding force for UVHG under different parameters when using the #100 tool are shown in **Fig.14**. When the feed rate and axial feed depth per helical revolution are constant, it can be found that the F_n decreases with the increase of spindle speed (**Fig.14a**). This is because the thickness and cross-sectional area of undeformed chip become smaller, and the volume of material removed by the tool per revolution becomes smaller in the same time, resulting in lower deformation resistance of the material and lower overall grinding force. When the spindle speed and axial feed depth per helical revolution are fixed, the F_n increases slightly with the increase of feed rate (**Fig.14b**). This is because the feed angle of the tool is approximately 1°-3° in UVHG, resulting in a very small axial feed component. Therefore, the axial force barely changes when feed rate rises. When the spindle speed and feed are fixed, the F_n increases remarkablly as the

axial feed depth per helical revolution increases (**Fig.14c**). The reason can be attributed to the increased undeformed chip thickness and cross-sectional area, and the volume of the material removed by the abrasive tool per unit time becomes larger, resulting in an increase in the axial grinding force. The average errors of the predicted and experimental values of the normal grinding force are 5.16%, 4.35%, and 6.99% for various spindle speed, feed rate, and axial feed depth per helical revolution, respectively, which were within the acceptable range. It is also found that the axial feed depth per helical revolution has a significant influence on the normal grinding force, followed by the spindle speed and feed rate.

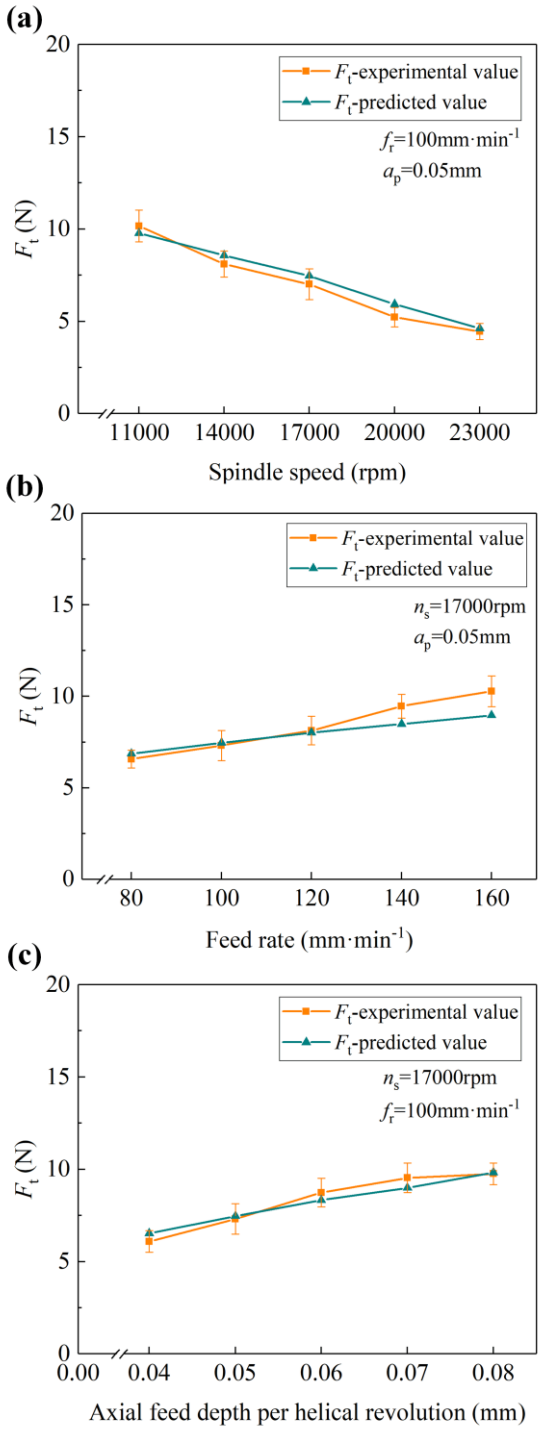

Fig.15. Experimental and predicted tangential grinding force under the experimental parameters

The predicted and experimental tangential grinding force for UVHG under different parameters are shown in **Fig.15**. Similar to the normal grinding force when the feed rate and axial feed depth per

helical revolution are kept constant, it can be found that the F_t decreases with the increase of the spindle speed (**Fig.15a**). When the spindle speed and axial feed depth per helical revolution are fixed, the F_t increases with the increase of feed rate (**Fig.15b**). In contrast to the normal force, the tangential force changes more remarkably with increasing feed rate due to its larger horizontal component. It is noteworthy that the deviation between the experimental and predicted values tends to expand when the feed rate reached 140 mm·min^{-1} and 160 mm·min^{-1}. This can be attributed to the increased number of lateral grains participating in grinding as the feed rate grows in actual machining.When the spindle speed and feed rate are fixed, the F_t increases with the increase of axial feed depth per helical revolution (**Fig.15c**). The average errors of the predicted and experimental values of the F_t are 5.84%, 6.21% and 4.08% for different spindle speed, feed rate and axial feed depth per helical revolution, respectively. It can also be found that the spindle speed and feed rate have a significant influence on the tangential grinding force.

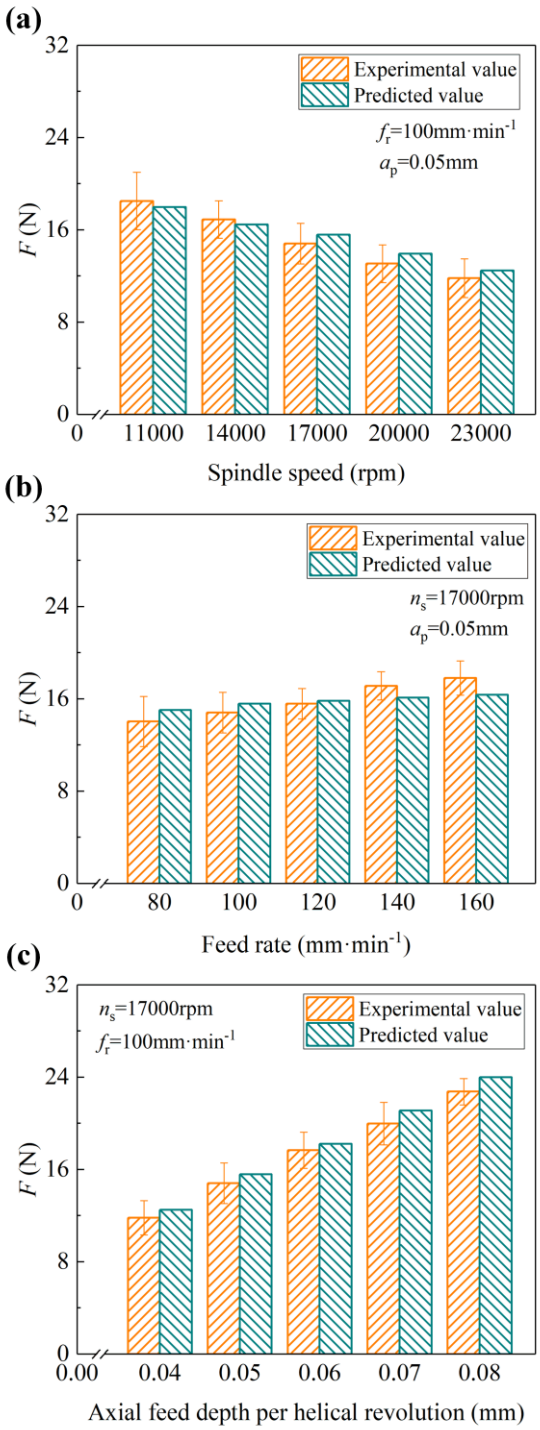

Fig.16. Experimental and predicted total grinding force of UVHG under the experimental parameters

The predicted and experimental results of the total grinding force of UVHG are shown in **Fig.16**. When the feed rate and axial feed depth per helical revolution are constant, the total grinding force decreases with the increase of spindle speed (**Fig.16a**). When the spindle speed increases from 11,000 rpm to 23,000 rpm, the grinding force decreased by 36.15%. When the spindle speed and axial feed depth per helical revolution are fixed, the total grinding force increases with the increase of feed rate (**Fig.16b**). When the feed rate increases from 80mm·min^{-1} to 160mm·min^{-1}, the grinding force increases by 26.84%. Similarly, the total grinding force increases with the increase of axial feed depth per helical revolution when the spindle speed and feed rate are constant (**Fig.16c**). When the axial feed depth per helical revolution increases from 0.04 mm to 0.08 mm, the grinding force increased

by 92.47%. Therefore, it can be found that the axial feed depth per helical revolution has the greatest influence on the total grinding force of all the experimental parameters in this research.

The deviation between the predicted and experimental values can be attributed to the particle size and distribution's randomness, as the particle greatly influences the fluctuation of grinding force [58]. In addition, the interface failure force between particles and matrix is neglected in the model, leading to some predicted values being smaller than the experimental value. Further, the arrangement and size of the diamond abrasive grits on the tool will affect the undeformed chip thickness and cross-sectional area, which also results in the model deviation. The average error between the predicted and experimental values of the total grinding force of the model within this study's experimental parameters is 5.07%. Compared with the literature [39,40,59,60], the model's prediction error is within the acceptable range, and the predicted result of the model agrees well with the experimental value. The model in this study has good accuracy and can be extended to be applied with other similar grinding tools in UVHG to guide the selection of parameters and process optimization.

4. Conclusion

A UVHG method is proposed for machining high-volume fraction SiC_p/Al composites. Considering the 'acoustic softening' effect caused by ultrasonic vibration on the SiC_p/Al composites, a model is established to predict the grinding force. The model is verified by UVHG experiments. The main conclusions are as follows:

(1) This study proposed a method for calculating the undeformed chip thickness and cross-sectional area in an ultrasonic vibration-assisted helical grinding process with a diamond abrasive tool. Not all the grits on the diamond abrasive tool participated in grinding, and the actual number of bottom and lateral grains involved is limited.

(2) The effects of ultrasonic vibration frequency and amplitude on the undeformed chip thickness and area are slight. But ultrasonic vibration can affect the deformation stress of the material. When the ultrasonic vibration power used in UVHG is 100%, the loading strain is $1*10^{-3}m{\cdot}s^{-1}$, and the compressive stress of SiC_p/Al composites decreases by 35.25%.

(3) Within the experimental parameter range, the predicted plastic deformation force accounts for at least 50% of the grinding forces. The proportion of friction force markedly increases with rising spindle speed. Both the normal and tangential grinding forces decrease with the increase of spindle speed while increasing with the increase of feed rate and axial feed depth per helical revolution. Due to the difference in feed components along the tangential and normal directions, its contribution to the axial force was limited. The axial feed depth per helical revolution exerts a greater influence on the grinding force.

(4) The UVHG force model exhibits average prediction deviations of 5.07% when using the #100 diamond abrasive tool, which is acceptable and can further guide the parameter selection and optimization of UVHG of SiC_p/Al composites.

Declarations

Ethics approval and consent to participate. The content studied in this article belongs to the field of metal matrix composites processing and does not involve humans and animals. This article strictly follows the accepted principles of ethical and professional conduct. The authors would like to opt in to In Review. The authors declare that they have no known competing financial interests or personal relationships that could have appeared to influence the work reported in this paper.

Acknowledgments

Author contribution

Qilin Li: methodology, investigation, experiments, writing of original draft, writing including review and editing, and visualization; Songmei Yuan: project administration and supervision; Xiaoxin Gao: model validation; Bochuan Chen: experiments; Zhen Li: review and editing; Muhammad Amin: language polishing; Andre D.L. Batako: review and editing; language polishing.

Funding

This work was supported by the National Natural Science Foundation of China [grant number U1737201] and the Science Center for Gas Turbine Project (P2022-A-IV-002-002).

References

[1]. Zhang X, Chen T, Ma S, Qin H, Ma J. Overcoming the strength-ductility trade-off of an aluminum matrix composite by novel core-shell structured reinforcing particulates. Composites Part B: Engineering 2021; 206:108541. https://doi.org/10.1016/j.compositesb.2020.108541.

[2]. Guo W, Hou J, Lin T, He P. Joining high volume fraction SiC particle reinforced aluminum matrix composites (SiCp/Al) by low melting point stannous oxide–zinc oxide–phosphorus pentoxide glass. Ceramics International 2021; 47:3955–63. https://doi.org/10.1016/j.ceramint.2020.09.259.

[3]. Zhang Q, Wu G, Chen G, Jiang L, Luan B. The thermal expansion and mechanical properties of high reinforcement content SiCp/Al composites fabricated by squeeze casting technology. Composites Part A: Applied Science and Manufacturing 2003; 34:1023–7. https://doi.org/10.1016/S1359-835X(03)00253-7.

[4]. Li X, Bai F, Fu Y. The small hole helical mill-grinding process and application in high volume fraction SiCp/Al MMCs. International Journal of Advanced Manufacturing Technology 2017; 91:3007–14. https://doi.org/10.1007/s00170-016-9941-1.

[5]. Yin G, Gong Y, Li Y, Song J, Zhou Y. Modeling and evaluation in grinding of SiCp/Al composites with single diamond grain. International Journal of Mechanical Sciences 2019; 163:105137. https://doi.org/10.1016/j.ijmecsci.2019.105137.

[6]. Yang Z, Zhu L, Zhang G, Ni C, Lin B. Review of ultrasonic vibration-assisted machining in advanced materials. International Journal of Machine Tools and Manufacture 2020; 156:103594. https://doi.org/10.1016/j.ijmachtools.2020.103594.

[7]. Wang B, Liu Z, Cai Y, Luo X, Ma H, Song Q, et al. Advancements in material removal mechanism and surface integrity of high speed metal cutting: A review. International Journal of Machine Tools and Manufacture 2021; 166:103744. https://doi.org/10.1016/j.ijmachtools.2021.103744.

[8]. Xiao X, Zheng K, Liao W, Meng H. Study on cutting force model in ultrasonic vibration assisted side grinding of zirconia ceramics. International Journal of Machine Tools and Manufacture 2016; 104:58–67. https://doi.org/10.1016/j.ijmachtools.2016.01.004.

[9]. Zhang B, Sui T, Lin B, Zheng W, Li S, Fang S, et al. Drilling process of Cf/SiC ceramic matrix composites: Cutting force modeling, machining quality and PCD tool wear analysis. Journal of Materials Processing Technology 2022; 304:117566. https://doi.org/10.1016/j.jmatprotec.2022.117566.

[10]. Tansel IN, Arkan TT, Smith D, McCool M. Tool wear estimation in micro-machining. International Journal of Machine Tools and Manufacture 2000; 40:599-608. https://doi.org/10.1016/S0890-6955(99)00073-5

[11]. Toubhans B, Fromentin G, Viprey F, Karaouni H, Dorlin T. Machinability of Inconel 718 during turning: Cutting

force model considering tool wear, influence on surface integrity. Journal of Materials Processing Technology 2020; 285:116809. https://doi.org/10.1016/j.jmatprotec.2020.116809.

[12]. Sur G, Motorcu AR, Nohutçu S. Single and multi-objective optimization for cutting force and surface roughness in peripheral milling of Ti6Al4V using fixed and variable helix angle tools. Journal of Manufacturing Processes 2022; 80:529–45. https://doi.org/10.1016/j.jmapro.2022.06.016.

[13]. Coelho RT, Yamada S, Aspinwall DK, Wise MLH. The application of polycrystalline diamond (PCD) tool materials when drilling and reaming aluminum based alloys including MMC. International Journal of Machine Tools and Manufacture 1995; 35:761–74. https://doi.org/10.1016/0890-6955(95)93044-7.

[14]. Ciftci I, Turker M, Seker U. CBN cutting tool wear during machining of particulate reinforced MMCs. Wear 2004; 257:1041–6. https://doi.org/10.1016/j.wear.2004.07.005.

[15]. Andrewes CJE, Feng H-Y, Lau WM. Machining of an aluminum/SiC composite using diamond inserts. Journal of Materials Processing Technology 2000; 102:25–9. https://doi.org/10.1016/S0924-0136(00)00425-8.

[16]. Huang S, Guo L, Yang H, Su Y, Xu L. Study on characteristics in high-speed milling SiCp/Al composites with small particles and high volume fraction by adopting PCD cutters with different grain sizes. International Journal of Advanced Manufacturing Technology 2019; 102:3563–71. https://doi.org/10.1007/s00170-019-03374-1.

[17]. Yingfei G, Jiuhua X, Hui Y. Diamond tools wear and their applicability when ultra-precision turning of SiCp/2009Al matrix composite. Wear 2010; 269:699–708. https://doi.org/10.1016/j.wear.2009.09.002.

[18]. Pramanik A. Developments in the non-traditional machining of particle reinforced metal matrix composites. International Journal of Machine Tools and Manufacture 2014; 86:44–61. https://doi.org/10.1016/j.ijmachtools.2014.07.003.

[19]. Zhang Z, Zhang Y, Lin L, Wu J, Yu H, Pan X, et al. study on productivity and aerosol emissions of magnetic field-assisted EDM process of SiC p / Al composite with high volume fractions. Journal of Cleaner Production 2021; 292:126018. https://doi.org/10.1016/j.jclepro.2021.126018.

[20]. Vinoth Kumar S, Pradeep Kumar M. Machining process parameter and surface integrity in conventional EDM and cryogenic EDM of Al–SiCp MMC. Journal of Manufacturing Processes 2015; 20:70–8. https://doi.org/10.1016/j.jmapro.2015.07.007.

[21]. Zhao G, Mao P, Li L, Iqbal A, He N. Micro-milling of 65 vol% SiCp/Al composites with a novel laser-assisted hybrid process. Ceramics International 2020; 46:26121–8. https://doi.org/10.1016/j.ceramint.2020.07.107.

[22]. Wei C, Guo W, Pratomo ES, Li Q, Wang D, Whitehead D, et al. High-speed, high-power density laser-assisted machining of Al-SiC metal matrix composite with significant increase in productivity and surface quality. Journal of Materials Processing Technology 2020; 285:116784. https://doi.org/10.1016/j.jmatprotec.2020.116784.

[23]. Zhao G, Hu M, Li L, Zhao C, Zhang J, Zhang X. Enhanced machinability of SiCp/Al composites with laser-induced oxidation assisted milling. Ceramics International 2020; 46:18592–600. https://doi.org/10.1016/j.ceramint.2020.04.169.

[24]. Savrun E, Taya M. Surface characterization of SiC whisker/2124 aluminum and Al_2O_3 composites machined by abrasive water jet[J]. Journal of Materials Science, 1988;23:1453-1458. https://doi.org/10.1007/BF01154616

[25]. Kadivar MA, Akbari J, Yousefi R, Rahi A, Nick MG. Investigating the effects of vibration method on ultrasonic-assisted drilling of Al/SiCp metal matrix composites. Robotics and Computer-Integrated Manufacturing 2014; 30:344–50. https://doi.org/10.1016/j.rcim.2013.10.001.

[26]. Dong G, Zhang H, Zhou M, Zhang Y. Experimental investigation on ultrasonic vibration assisted turning of Sicp/Al composites. Materials and Manufacturing Processes 2012; 28: 999-1002, https://doi.org/10.1080/10426914.2012.709338.

[27]. Zhou J, Lu M, Lin J, Zhou X, Guo M, Du Y. Investigation of surface integrity transition of SiCp/Al composites based on specific cutting energy during ultrasonic elliptical vibration assisted cutting. Journal of Manufacturing Processes 2022; 79:654–65. https://doi.org/10.1016/j.jmapro.2022.04.067.

[28]. Dong Z, Zheng F, Zhu X, Kang R, Zhang B, Liu Z. Characterization of material removal in ultrasonically assisted grinding of SiCp/Al with high volume fraction. International Journal of Advanced Manufacturing Technology 2017; 93:2827–39. https://doi.org/10.1007/s00170-017-0676-4.

[29]. Fan Y, Xu Y, Hao Z, Lin J. Cutting deformation mechanism of SiCp/Al composites based on strain gradient theory. Journal of Materials Processing Technology 2022; 299:117345. https://doi.org/10.1016/j.jmatprotec.2021.117345.

[30]. Liu G, Xiang D, Peng P, Li Y, Yuan Z, Zhang Z, et al. Establishment of scratching force model for micro-removal of SiCp/Al composites by ultrasonic vibration. Journal of Materials Processing Technology 2022; 307:117677. https://doi.org/10.1016/j.jmatprotec.2022.117677.

[31]. Liu C, Gao L, Jiang X, Xu W, Liu S, Yang T. Analytical modeling of subsurface damage depth in machining of SiCp/Al composites. International Journal of Mechanical Sciences 2020; 185:105874. https://doi.org/10.1016/j.ijmecsci.2020.105874.

[32]. Chen G, Ren C, Zou Y, Qin X, Lu L, Li S. Mechanism for material removal in ultrasonic vibration helical milling of Ti 6Al 4V alloy. International Journal of Machine Tools and Manufacture 2019; 138:1–13. https://doi.org/10.1016/j.ijmachtools.2018.11.001.

[33]. Liu D, Cong WL, Pei ZJ, Tang Y. A cutting force model for rotary ultrasonic machining of brittle materials. International Journal of Machine Tools and Manufacture 2012; 52:77–84. https://doi.org/10.1016/j.ijmachtools.2011.09.006.

[34]. Wang J, Feng P, Zhang J, Zhang C, Pei Z. Modeling the dependency of edge chipping size on the material properties and cutting force for rotary ultrasonic drilling of brittle materials. International Journal of Machine Tools and Manufacture 2016; 101:18–27. https://doi.org/10.1016/j.ijmachtools.2015.10.005.

[35]. Wang J, Zhang J, Feng P, Guo P. Experimental and theoretical investigation on critical cutting force in rotary ultrasonic drilling of brittle materials and composites. International Journal of Mechanical Sciences 2018; 135:555–64. https://doi.org/10.1016/j.ijmecsci.2017.11.042.

[36]. Xiao X, Zheng K, Liao W, Meng H. Study on cutting force model in ultrasonic vibration assisted side grinding of zirconia ceramics. International Journal of Machine Tools and Manufacture 2016; 104:58–67. https://doi.org/10.1016/j.ijmachtools.2016.01.004.

[37]. Wang H, Hu Y, Cong W, Hu Z. A mechanistic model on feeding-directional cutting force in surface grinding of CFRP composites using rotary ultrasonic machining with horizontal ultrasonic vibration. International Journal of Mechanical Sciences 2019; 155:450–60. https://doi.org/10.1016/j.ijmecsci.2019.03.009.

[38]. Wang H, Pei ZJ, Cong W. A mechanistic cutting force model based on ductile and brittle fracture material removal modes for edge surface grinding of CFRP composites using rotary ultrasonic machining. International Journal of Mechanical Sciences 2020; 176:105551. https://doi.org/10.1016/j.ijmecsci.2020.105551.

[39]. Lu S, Gao H, Bao Y, Xu Q. A model for force prediction in grinding holes of SiCp/Al composites. International Journal of Mechanical Sciences 2019; 160:1–14. https://doi.org/10.1016/j.ijmecsci.2019.06.025.

[40]. Zhou M, Zheng W. A model for grinding forces prediction in ultrasonic vibration assisted grinding of SiCp/Al composites. International Journal of Advanced Manufacturing Technology 2016; 87:3211–24. https://doi.org/10.1007/s00170-016-8726-x.

[41]. Fartashvand V, Abdullah A, Sadough Vanini SA. Investigation of Ti-6Al-4V alloy acoustic softening. Ultrasonics Sonochemistry 2017; 38:744–9. https://doi.org/10.1016/j.ultsonch.2016.07.007.

[42]. Yao Z, Kim G-Y, Wang Z, Faidley L, Zou Q, Mei D, et al. Acoustic softening and residual hardening in aluminum: Modeling and experiments. International Journal of Plasticity 2012; 39:75–87. https://doi.org/10.1016/j.ijplas.2012.06.003.

[43]. Verma GC, Pandey PM, Dixit US. Estimation of workpiece-temperature during ultrasonic-vibration assisted milling considering acoustic softening. International Journal of Mechanical Sciences. 2018; 140:547–56. https://doi.org/10.1016/j.ijmecsci.2018.03.034.

[44]. Wang CJ, Liu Y, Guo B, Shan DB, Zhang B. Acoustic softening and stress superposition in ultrasonic vibration assisted uniaxial tension of copper foil: Experiments and modeling. Materials & Design 2016; 112:246–53. https://doi.org/10.1016/j.matdes.2016.09.042.

[45]. Zhang B, Yin J. The 'skin effect' of subsurface damage distribution in materials subjected to high-speed machining. International Journal of Extreme Manufacturing. 2019; 1:012007. https://doi.org/10.1088/2631-7990/ab103b.

[46]. Yang X, Zhang B. Material embrittlement in high strain-rate loading. International Journal of Extreme Manufacturing. 2019; 1:022003. https://doi.org/10.1088/2631-7990/ab263f.

[47]. Verma GC, Pandey PM, Dixit US. Modeling of static machining force in axial ultrasonic-vibration assisted milling considering acoustic softening. International Journal of Mechanical Sciences 2018; 136:1–16. https://doi.org/10.1016/j.ijmecsci.2017.11.048.

[48]. Zai P, Tong J, Liu Z, Zhang Z, Song C, Zhao B. Analytical model of exit burr height and experimental investigation on ultrasonic-assisted high-speed drilling micro-holes. Journal of Manufacturing Processes 2021; 68:807–17. https://doi.org/10.1016/j.jmapro.2021.06.010.

[49]. Malkin S. Grinding Technology: Theory and Applications of Machining with Abrasives. International Journal of Machine Tools and Manufacture, 1991, 31(3):435-436.https://doi.org/10.1016/0890-6955(91)90088-K

[50]. Zhang Y, Li C , Ji H , et al. analysis of grinding mechanics and improved predictive force model based on material-removal and plastic-stacking mechanisms. International Journal of Machine Tools and Manufacture, 2017, 122:81-97. https://doi.org/10.1016/j.ijmachtools.2017.06.002.

[51]. Wu Q , Xu W , Zhang L C . Machining of particulate-reinforced metal matrix composites: An investigation into the chip formation and subsurface damage. Journal of Materials Processing Technology, 2019, 274. https://doi.org/10.1016/j.jmatprotec.2019.116315

[52]. Griffith A A . The Phenomena of Rupture and Flow in Solids. Philosophical Transactions of The Royal Society A Mathematical Physical and Engineering Sciences, 1920, A221(4):163-198. https://doi.org/10.1098/rsta.1921.0006

[53]. Lawn B R , Evans A G . A model for crack initiation in elastic/plastic indentation fields. Journal of Materials Science, 1977, 12(11):2195-2199. https://doi.org/10.1007/BF00552240

[54]. Tohgo K, Itoh T. Elastic and elastic-plastic singular fields around a crack-tip in particulate-reinforced composites with progressive debonding damage. Int J Solids Struct 2005;42(26):6566–85. https://doi.org/10.1016/j.ijsolstr.2005.04.013.

[55]. Duan C, Sun W, Fu C, et al. Modeling and Simulation of Tool-Chip Interface Friction in Cutting Al/SiC_p Composites based on A Three-phase Friction Model. International Journal of Mechanical Sciences, 2018, s142–143:384-396. https://doi.org/10.1016/j.ijmecsci.2018.05.014

[56]. Inman D J . Reduction of friction using piezoelectrically excited ultrasonic vibrations. Smart Structures & Materials: Damping & Isolation. Smart Structures and Materials 2001: Damping and Isolation, 2001. https://doi.org/10.1117/12.432714

[57]. Li Z, Li X, Huang Z, Zhang Z, et al. Ultrasonic-vibration-enhanced plasticity of an entropic alloy at room

temperature. Acta Materialia 2022; 225:117-569. https://doi.org/10.1016/j.actamat.2021.117569

[58]. C. Liu, W. Ding, T. Yu, C. Yang, Materials removal mechanism in high-speed grinding of particulate reinforced titanium matrix composites, Precis Eng. 51 (2018) 68–77. https://doi.org/10.1016/j.precisioneng.2017.07.012

[59]. Sikder S, Kishawy H A. Analytical model for force prediction when machining metal matrix composite. International Journal of Mechanical Sciences, 2012, 59(1):95-03. https://doi.org/10.1016/j.ijmecsci.2012.03.010

[60]. Ghandehariun A, Hussein H M, Kishawy H A. Machining metal matrix composites: Novel analytical force model. International Journal of Advanced Manufacturing Technology, 2016, 83(1-4):233-241. https://doi.org/10.1007/s00170-015-7554-8